INTERNATIONAL JOURNAL FOR NUMERICAL METHODS IN FLUIDS
Int. J. Numer. Meth. Fluids **29**: 465–483 (1999)

AN IMPROVED TECHNIQUE FOR SOLVING TWO-DIMENSIONAL SHALLOW WATER PROBLEMS

S. GUILLOU* AND K.D. NGUYEN

Laboratoire de Mécanique de Caen, Université de Caen, Caen, France

SUMMARY

A numerical model for solving the 2D shallow water equations is proposed herewith. This model is based on a finite volume technique in a generalized co-ordinate system, coupled with a semi-implicit splitting algorithm in which a Helmholtz equation is used for the surface elevation. Several benchmark problems have proven the good accuracy of this method in complex geometries. Nevertheless, several numerical perturbations were noted in the surface elevation. After finding the origin, a new numerical technique is suggested, to avoid these perturbations. Several severe tests are proposed to validate this technique. Copyright © 1999 John Wiley & Sons, Ltd.

KEY WORDS: shallow water equations; numerical model; checkerboard; curvilinear co-ordinates; finite volume method; collocated arrangement

1. INTRODUCTION

Over the past 20 years, finite volume techniques have been considerably developed to solve the Navier–Stokes equations. A Cartesian staggered grid [34], suitable to ensure mass and momentum conservation, has been frequently used. But for the real applications, we have been confronted by a real problem: the complex morphology of the fluid domain needs a very fine computing grid to model the studied zone with accuracy. This unacceptably increases the computing cost and CPU memory requirement. In recent years, body-fitting co-ordinate (BFC) techniques have, therefore, been proposed in order to overcome this difficulty. BFC techniques applied to solve Navier–Stokes equations have been offered by Karki and Patankar [1] for 2D and then by Nguyen *et al.* [2] for 3D arbitrary geometries. They have used the SIMPLE technique [3] coupled with a staggered grid and covariant velocity components as depending variables. Cartesian velocity components in a staggered grid using the fractional step or the projection method have also been proposed [4]. However, the curvilinear staggered grid techniques present important difficulties. Indeed, Zang *et al.* [4] calculated the pressure at the cell center and nine Cartesian velocity components at three cell-face centers. The metric tensors defined at the center, as well as the midpoint of three cell-faces and the midpoint of the three edges, must be kept in CPU memory. As a consequence, the computing cost and the CPU memory requirement are quite large. Karki and Patankar [1] and Nguyen *et al.* [2] calculated one covariant velocity component at each cell-face. Since only three momentum equations

---

* Correspondence to: Laboratoire de Mécanique de Caen, Université de Caen, Campus II, Bd. MP. JUIN, BP5186, 14032 Caen, France. E-mail: guillou@meca.unicaen.fr

CCC 0271–2091/99/040465–19$17.50

Received January 1997
Revised December 1997

instead of nine need to be solved, the computing time is considerably diminished. But this requires special interpolations to obtain other velocity components wanted to couple with the pressure-linked equation. The result is that the interpolation may produce truncation errors in the numerical solution, especially in complex and singular geometries.

In order to avoid the above mentioned disadvantages, the curvilinear non-staggered grid techniques have greatly evolved. But, as shown by Rhie and Chow [5], this technique coupled with Chorin's projection method [6] produces spurious oscillations in the pressure field. This is the so-called *checkerboard* pattern. It seems that numerically, in a non-staggered grid technique, a straightforward discretization of the continuity equation causes a pressure field decoupling. There exists two networks of pressure nodes, thus producing the odd–even solution for the pressure. Guermond [7,8] showed mathematically the origin of the checkerboard by solving the incompressible Navier–Stokes equations using Chorin's method and demonstrated that the *Inf–sup* condition must be taken as a necessary criterion to ensure the removal of these oscillations. Rhie and Chow [5] used the intermediate volume fluxes, determined on the cell-faces by an upwind interpolation to calculate steady flows. This numerically respects the *Inf–sup* condition and thus prevents numerical oscillations. Zang *et al.* [9] extended Rhie and Chow's method to calculate unsteady flows. Deng *et al.* [10] proposed another approach using the SIMPLE method. They used a Consistent Physical Interpolation (CPI) to reconstruct the velocity fluxes on the cell-faces from the mass and momentum equations. This allows the use of a non-staggered grid without producing the spurious pressure oscillations.

When calculating coastal and estuarine flows, the above mentioned difficulties have also been met. Until now, most coastal and estuarine models were based on either the Cartesian staggered finite volume methods [11–14] or the finite element methods [15]. Nowadays, the use of a Cartesian finite volume method has become more and more unacceptable as a means to calculate geometrically complex coastal flows. This can be explained by the fact that the development of the marine sciences needs the long-term and circulation simulation to be coupled with the biological and ecological models. As for the finite element models, they also produce the checkerboard [16,17] if no special technique that ensures the *Inf–sup* condition is used.

This paper presents a non-staggered grid technique coupled with the fractional step method to solve the two-dimensional shallow water equations. Sections 2 and 3 present the governing equation in a non-orthogonal curvilinear co-ordinate system. The numerical technique is presented in Section 4. In Section 5, the proposed technique is tested by several benchmark tests and the results obtained are discussed. In Section 6, an attempt is made to discover the numerical, such as pollution, spurious oscillations in the pressure fields and to show its origin. A technique is proposed to avoid the numerical pollution in Section 6.2. Finally, the results of the benchmark for the proposed anti-pollution technique are presented and discussed in Section 6.3.

2. 2D SHALLOW WATER EQUATIONS

The objective is the simulation of coastal and estuarine flows. For this, the hydrostatic pressure approximation is used. This one permits the use of the surface elevation instead of the pressure. If the fluid domain is vertically well-mixed, the integration of the Navier–Stokes equation (NSE) over the water depth gives the following:

$$\begin{cases} \dfrac{\partial \eta}{\partial t} + \vec{\nabla}\cdot\vec{Q} = 0 \\ \dfrac{\partial \vec{Q}}{\partial t} + \vec{\nabla}\cdot(\vec{U}\otimes\vec{Q} - A_H\vec{\nabla}\vec{Q}) + gH\vec{\nabla}\eta - \dfrac{\tau_\mathrm{b}}{\rho_\mathrm{r}} = 0 \end{cases}. \tag{1}$$

Equation (1) is the 2D shallow water equation (SWE). As indicated in Figure 1, η represents the water surface elevation, h is the bed level, while $H = h + \eta$ is the water depth. $\vec{U} = (U_1, U_2)$ and $\vec{Q} = H\vec{U} = (Q_1, Q_2)$ are respectively, the depth average velocity and the unit width discharge. ρ_r is the water density reference. A_H is the horizontal diffusion coefficient. $(\tau_{\mathrm{b}1}, \tau_{\mathrm{b}2})$ represents the bed shear stress. Commonly, this parameter is linked to the depth average velocity by a quadratic law.

$$\vec{\tau}_\mathrm{b} = (\tau_{\mathrm{b}1}, \tau_{\mathrm{b}2}) = \rho_\mathrm{r}\frac{C_f}{2}\vec{U}\sqrt{U_1^2 + U_2^2} = \rho_\mathrm{r}F_\mathrm{b}\vec{Q}. \tag{2}$$

In this relation, C_f is the Darcy coefficient given by some empirical relations. Afterwards, it will be noted that $F_\mathrm{b} = (C_f/2H)\sqrt{U_1^2 + U_2^2}$.

3. THE CURVILINEAR CO-ORDINATE SYSTEM

3.1. Definition

Note that $\{x_i\}$ is the Cartesian base and that $\{\xi^i\}$ is the curvilinear base *a priori* non-orthogonal. Using the covariant $\{\vec{a}_i\}$ and the contravariant $\{\vec{a}^i\}$ bases, another contravariant base $\{\vec{b}^i\}$ is defined by ($\wedge$ is the vectorial product):

$$\vec{b}^i = J\vec{a}^i = \vec{a}_j \wedge \vec{a}_k = \frac{\partial \vec{x}}{\partial \xi^j} \wedge \frac{\partial \vec{x}}{\partial \xi^k} \quad (i, j, k) = \{(1, 2, 3);\ (2, 3, 1);\ (3, 1, 2)\}. \tag{3}$$

In a two-dimensional space, vectors $\vec{b}^i$ read:

$$(b_j^i) = J\begin{pmatrix} \xi^1_{x_1} & \xi^2_{x_1} \\ \xi^1_{x_2} & \xi^2_{x_2} \end{pmatrix} = \begin{pmatrix} x_{2\xi^2} & -x_{2\xi^1} \\ -x_{1\xi^2} & x_{1\xi^1} \end{pmatrix}, \tag{4}$$

where J represents the Jacobian of the transformation and:

$$J = \vec{a}_i\cdot(\vec{a}_j \wedge \vec{a}_k) = b_1^1 b_2^2 - b_2^1 b_1^2. \tag{5}$$

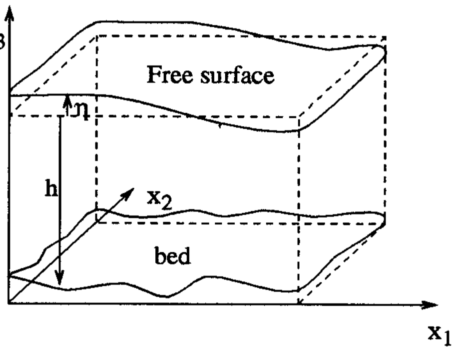

Figure 1. Definition sketch.

3.2. The equations

Using these conditions, Equation (1) is transformed as:

$$\begin{cases} \dfrac{\partial \eta}{\partial t} + \dfrac{1}{J}\dfrac{\partial}{\partial \xi^j} Q^j = 0, \\ \dfrac{\partial Q_i}{\partial t} + \dfrac{1}{J}\dfrac{\partial}{\partial \xi^j}\left(U^j Q_i - d_{jl}\dfrac{\partial Q_i}{\partial \xi^l}\right) + gH\dfrac{b_i^j}{J}\dfrac{\partial \eta}{\partial \xi^j} + F_b Q_i = 0. \end{cases} \tag{6}$$

where, $U^j = \vec{b^j}\cdot\vec{U}$ represents the jth velocity contravariant component, $d_{jl} = ((\vec{b^j}\cdot\vec{b^l})/J)A_H$ is the diffusion metric tensor, $Q^j = \vec{b^j}\cdot\vec{Q}$ is the jth unit width discharge contravariant component, and Q_i is the ith unit width discharge Cartesian component.

The choice of the Cartesian components as dependent variables allows the treatment of Equation (6) without the Christofel symbol. Thus, the numerical model is simplified.

4. INITIAL FINITE VOLUME METHOD AND SPLITTING ALGORITHM

4.1. Algorithm

The system of equations is solved by the fractional step technique (see Nguyen and Ouashine [18], Benqué *et al.* [11]) in three steps. In the first step, the advection–diffusion problem is solved with the source term, where the unknown is the intermediate unit width $\tilde{Q}_i^{k+1}$ (k represents the time step, with $t = k\Delta t$). In the second one, the wave propagation step, a Helmholtz's equation is constructed to obtain the elevation at a new time step, $k+1$, while in the third one, the new unit width discharge components Q_i^{k+1} are calculated from the elevation gradient.

A semi-implicit θ scheme [19] is used. Thus, the weight coefficients θ_{D} for the advection–diffusion step, and θ_{P} for the propagation step are introduced.

- The advection–diffusion step is:

$$\frac{\delta Q_i}{\Delta t} + \theta_{\mathrm{D}}\frac{1}{J}\frac{\partial}{\partial \xi^j}\left(U^j \delta Q_i - d_{jj}\frac{\partial \delta Q_i}{\partial \xi^j}\right) = -\frac{1}{J}\frac{\partial}{\partial \xi^j}\left(U^j Q_i^k - d_{jl}\frac{\partial Q_i^k}{\partial \xi^j}\right), \tag{7}$$

  with $\delta Q_i = \tilde{Q}_i^{k+1} - Q_i^k$, for $i = 1, 2$ and $j = 1, 2$.

- The propagation step is:

$$\left(K_3 - \frac{\theta_{\mathrm{P}}^2}{J}\frac{\partial}{\partial \xi^j} G_{jj}\frac{\partial}{\partial \xi^j}\right)\delta\eta = \frac{\theta_{\mathrm{P}}}{J}\frac{\partial}{\partial \xi^j} G_{jl}\frac{\partial \eta^k}{\partial \xi^l} - \frac{1}{J}\frac{\partial}{\partial \xi^j}\left(\frac{1}{\Delta t}\vec{b^j}\cdot\vec{\tilde{Q}}^{k+1}\right), \tag{8}$$

  where $G_{jl} = ((\vec{b^j}\cdot\vec{b^l})/J)gH$, $\delta\eta = \eta^{k+1} - \eta^k$, $K_4 = 1 + \theta_{\mathrm{P}} F_{\mathrm{b}}\Delta t$ and $K_3 = K_4/\Delta t^2$.

- The correction step is:

$$Q_i^{k+1} = \left(K_5 \tilde{Q}_i^{k+1} - gH\Delta t\frac{b_i^j}{J}\frac{\partial}{\partial \xi^j}(\theta_{\mathrm{P}}\eta^{k+1} + (1-\theta_{\mathrm{P}})\eta^k)\right)/K_4, \tag{9}$$

  where $K_5 = 1 - \Delta t F_{\mathrm{b}}(1 - \theta_{\mathrm{P}})$ and $i = 1, 2$.

This method seems similar to the well-known *projection algorithm* initially proposed by Chorin [6] and Temam [20] for the Navier–Stokes equations. However, Guillou [21] showed that the accuracy of the present method to calculate the water elevation is $O(\Delta t^2)$, while the

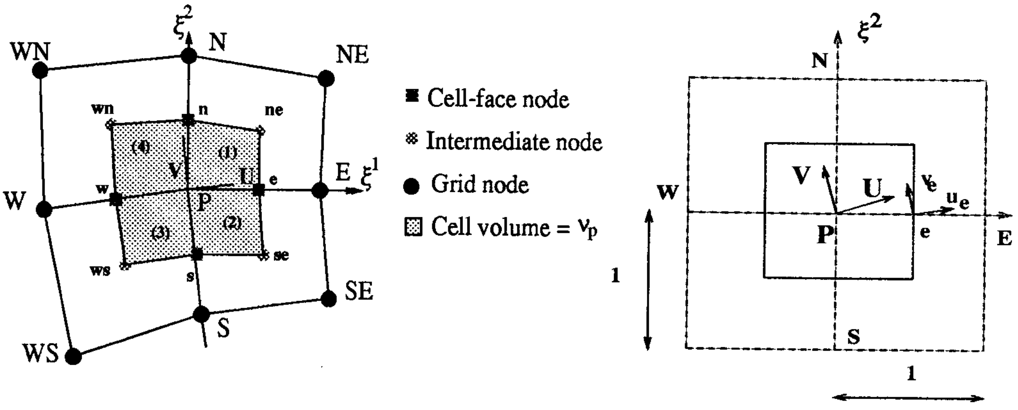

a) **Physical plane**

b) **transformed plane**

Figure 2. Cell definition.

pressure accuracy is $O(\Delta t^{1/2})$ when Chorin's [6] method is used. This is due to the presence of the time derivative of the water elevation in the continuity equation.

4.2. *Finite volume technique*

The finite volume method (FVM) is used to discretize the different steps. The control volume $\mathcal{V}_p$ is defined by Figure 2. All the variables (Q_1, Q_2, η) are placed at the grid nodes. This allows the use of only one control volume for all the equations.

The transport equation of a scalar variable ϕ, which can represent Q_1, Q_2 or η, can be written as follows:

$$\int_{\mathcal{V}_p} \frac{\partial \phi}{\partial t}\,\mathrm{d}V + \int_{\mathcal{V}_p} \frac{1}{J}\frac{\partial}{\partial \xi^i}(\vec{b}^i \cdot \vec{F})\,\mathrm{d}V = \int_{\mathcal{V}_p} S\,\mathrm{d}V, \tag{10}$$

where $\mathrm{d}V = \mathrm{d}x\,\mathrm{d}y = J\,\mathrm{d}\xi^1\,\mathrm{d}\xi^2$ and $\vec{F}$ is the ϕ flux vector. Discretizing Equation (10) gives

$$\frac{\phi^{k+1} - \phi^k}{\Delta t}V + I_e(\phi^{k+1}, \phi^k) - I_w(\phi^{k+1}, \phi^k) + I_n(\phi^{k+1}, \phi^k) - I_s(\phi^{k+1}, \phi^k)$$

$$= \int_{\mathcal{V}_p} S^{k+1}\,\mathrm{d}V. \tag{11}$$

The quantity I_e represents the total ϕ flux crossing the cell-face [ne, se]. For an advective flux $(\vec{F} = \vec{U}\phi)$, you have

$$I_e = \frac{1}{2}(\vec{b}^1_{ne} + \vec{b}^1_{se}) \cdot \vec{U}_e \phi_e, \tag{12}$$

and for a diffusive flux $(\vec{F} = (\partial\phi/\partial x_1, \partial\phi/\partial x_2))$:

$$I_e = \frac{1}{2}\left(\left(\frac{\vec{b}^1 \cdot \vec{b}^1}{J}\right)_{ne} + \left(\frac{\vec{b}^1 \cdot \vec{b}^1}{J}\right)_{se}\right)(\phi_E - \phi_P) + \left(\frac{\vec{b}^1 \cdot \vec{b}^2}{J}\right)_{ne}(\phi_{ne} - \phi_e) + \left(\frac{\vec{b}^1 \cdot \vec{b}^2}{J}\right)_{se}(\phi_e - \phi_{se}). \tag{13}$$

The treatment of the advective term needs particular care. So, the Hybrid scheme ([3], p. 88) is used to avoid the numerical perturbations appearing when a central difference scheme is used.

4.3. Decomposition technique

A decomposing technique has been used to solve Equations (7) and (8). As an example, Equation (8) can be successively decomposed into the ξ^1- and the ξ^2-directions as follows:

$$\begin{cases} \left(1-\dfrac{\theta_{\mathrm{P}}^2}{JK_3}\dfrac{\partial}{\partial\xi^1}G_{11}\dfrac{\partial}{\partial\xi^1}\right)\delta\eta^* = \dfrac{1}{JK_3}\dfrac{\partial}{\partial\xi^j}\left(\theta_{\mathrm{P}}G_{jl}\dfrac{\partial\eta^k}{\partial\xi^l}-\dfrac{1}{\Delta t}\vec{b}^j\cdot\vec{\tilde{Q}}^{k+1}\right), \\ \left(1-\dfrac{\theta_{\mathrm{P}}^2}{JK_3}\dfrac{\partial}{\partial\xi^2}G_{22}\dfrac{\partial}{\partial\xi^2}\right)\delta\eta = \delta\eta^*. \end{cases} \tag{14}$$

So, one is able to solve two 1D instead of one 2D problems. Thus, the calculating algorithm is simplified. The use of the above mentioned discretization technique (14) yields two tridiagonal systems that can easily be solved by a double sweep technique. Nevertheless, this decomposition produces a truncation error E_f, which is written as:

$$E_f = \frac{\theta_{\mathrm{P}}^2}{JK_3}\frac{\partial}{\partial\xi^1}G_{11}\frac{\partial}{\partial\xi^1}\frac{\theta_{\mathrm{P}}^2}{JK_3}\frac{\partial}{\partial\xi^2}G_{22}\frac{\partial}{\partial\xi^2}\delta\eta. \tag{15}$$

In the case of orthogonal mesh and regular bathymetry, E_f can be simplified as:

$$E_f = \left(\frac{\theta_{\mathrm{P}}^2}{JK_3}\right)^2 G_{11}G_{22}\frac{\partial^2}{\partial\xi^{1^2}}\frac{\partial^2}{\partial\xi^{2^2}}\delta\eta = \left(\frac{\theta_{\mathrm{P}}^2 gH}{JK_3}\right)^2((\xi^2_{x_1})^2+(\xi^1_{x_2})^2)((\xi^2_{x_1})^2+(\xi^2_{x_2})^2)\frac{\partial^2}{\partial\xi^{1^2}}\frac{\partial^2}{\partial\xi^{2^2}}\delta\eta. \tag{16}$$

Note that $\Delta^4(\delta\eta^{n+1})$ is the discrete form of $(\partial^2/\partial\xi^{1^2})(\partial^2/\partial\xi^{2^2})\delta\eta^{n+1}$. Moreover, in a regular Cartesian grid, one has $\partial\xi^i/\partial x_j = 1/\Delta x_j$ if $i=j$ and $\partial\xi^i/\partial x_j = 0$. If $i \neq j$, E_f is estimated by:

$$E_f \approx \frac{\theta_{\mathrm{P}}^4\Delta t^4(gH)^2}{(1+\theta_{\mathrm{P}}F_{\mathrm{b}}\,\mathrm{d}t)^2}\frac{1}{\Delta x_1^2}\frac{1}{\Delta x_2^2}\Delta^4(\delta\eta) \leq \frac{\theta_{\mathrm{P}}^4}{(1+\theta_{\mathrm{P}}F_{\mathrm{b}}\,\mathrm{d}t)^2}Ct^4\Delta^4(\delta\eta). \tag{17}$$

Ct is the Courant number for the gravity wave propagation, defined as:

$$Ct = \Delta t\sqrt{gH}\sqrt{\frac{1}{\Delta x_1^2}+\frac{1}{\Delta x_2^2}}. \tag{18}$$

Note that E_f is proportional to Ct^4. This implies that the bigger Ct is, the more important E_f is. Thus, it is better not to use a too large Ct.

5. ACADEMIC TESTS AND RESULTS

In this section, the proposed method will be validated by some benchmark tests.

Thus, two benchmark problems are presented here. The objective of the first one is to simulate gravity wave propagation, such as a tidal one, in a distorted geometry during a long-time. In this case, the advective, diffusive and Coriolis effects are left aside. The second test considers a jet-forced flow in a circular reservoir. In the latter case, the advective and diffusive effects are taken into account.

5.1. Polar basin

Let the study be of a flow in a polar basin closed on three sides. A distorted mesh of 21 × 41 points (Figure 3(a)) has been imposed. The basin has the form of a quarter annulus, the internal radius of which is $R_1 = 100$ km, and the external radius of which is $R_2 = 200$ km. At the open boundary, a tidal-forced function, $\eta(t) = \eta_0 \cos \omega t$ of period $T = 12.4$ h, and of amplitude $\eta_0 = 0.1$ m is imposed. Clearly, η is independent of the polar angle. A slip condition was used at the lateral walls. Darcy's coefficient was fixed at $C_f = 9.81 \times 10^{-3}$, while the bed level is assumed in a function of the radius, and is given by:

$$h = h_0 r^{-2}, \qquad h_0 = 8 \times 10^{11}\ \text{m}^3.$$

The water elevation is determined by Equation (8), or after a decomposing technique by Equation (14) using the implicit finite volume scheme presented in Section 4.2. The velocity is calculated using Equation (9). The analytical solution of this problem, without advection and diffusion effects, is given by [22]:

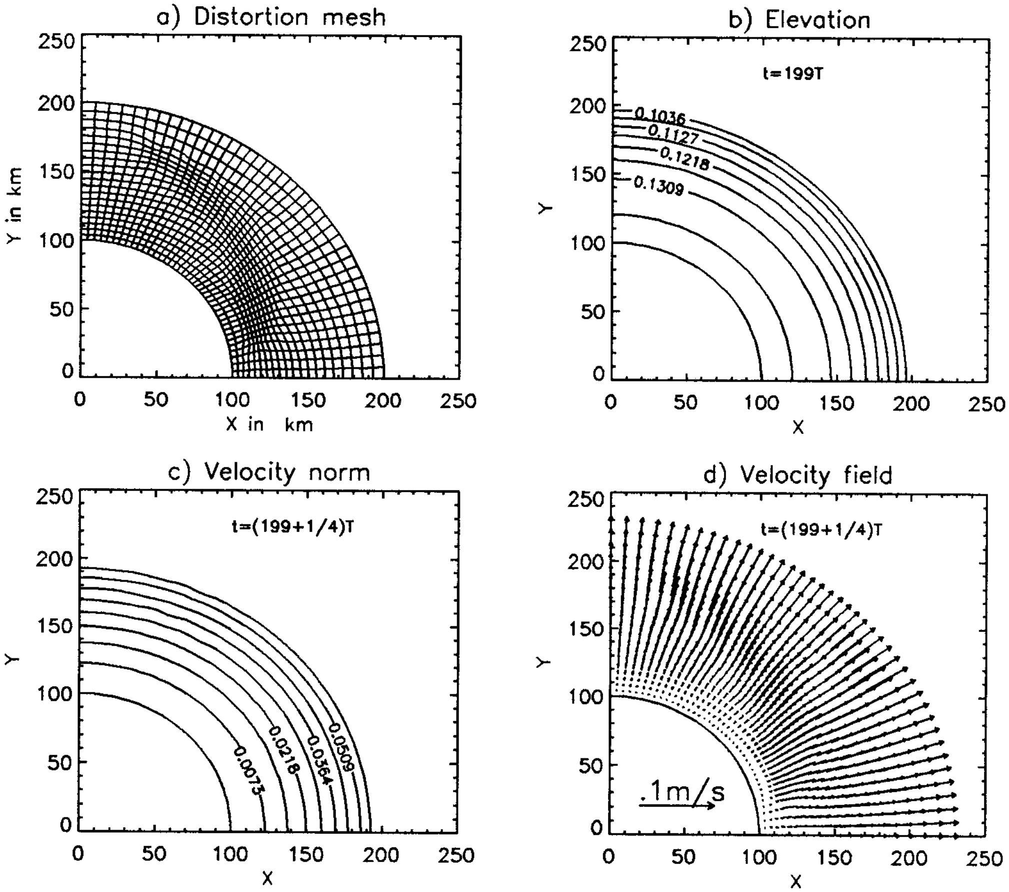

Figure 3. Polar channel: mesh and results.

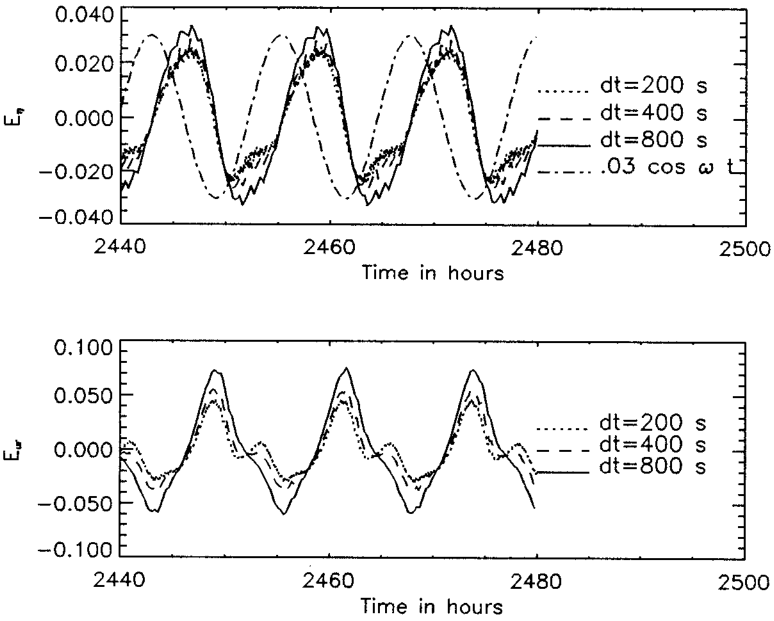

Figure 4. Relative error in η and U_r at point (9844 km, 106 km).

$$\begin{cases} \eta(r,t) = Re\left\{\eta_0 \dfrac{\cos(\frac{1}{2}\beta(r^2 - r_1^2))}{\cos(\frac{1}{2}\beta(r_2^2 - r_1^2))}\, e^{i\omega t}\right\} \\ U_r(r,t) = Re\left\{-\dfrac{i\omega r \eta_0}{h_0\beta}\, \dfrac{\sin(\frac{1}{2}\beta(r^2 - r_1^2))}{\cos(\frac{1}{2}\beta(r_2^2 - r_1^2))}\, e^{i\omega t}\right\}. \\ \beta^2 = \dfrac{\omega^2 - i\omega\tau}{gh_0}, \qquad c = \sqrt{gh} \end{cases} \tag{19}$$

The time steps of 200, 400 and 800 s are used, a parameter $\theta_P = 0.7$ and a time simulation of 200 tidal cycles being chosen.

In Figure 3(b)–(d), the contour map of surface elevation at time $t = 199T$, the velocity norm, and the velocity field at time $t = 199T + T/4$ (middle of the ebb period) can be seen. These figures show first that the solution is effectively independent of the polar angle, and secondly, that the mesh distortion does not affect the numerical solution.

A comparison was made between the analytical and numerical solution at the reference point (98.41 km, 106 km). Figure 4 shows the diagram of the relative error in the elevation and the radial velocity u_r: $E_\eta = (\eta - \eta_{ex})/\max(\eta_{ex}(t))$, $E_{U_r} = (U_r - U_{ex})/\max(U_{ex}(t))$. In addition, the temporal signal of the analytical elevation has been drawn. This shows that error is in contrast with the analytical signal. Thus, the error is principally due to a phasis error.

Table I. Maximum relative errors for the polar basin

Δt (s)	200	400	800
E_η (%)	2.6	2.7	3.2
E_{U_r} (%)	4.4	5.6	7.4

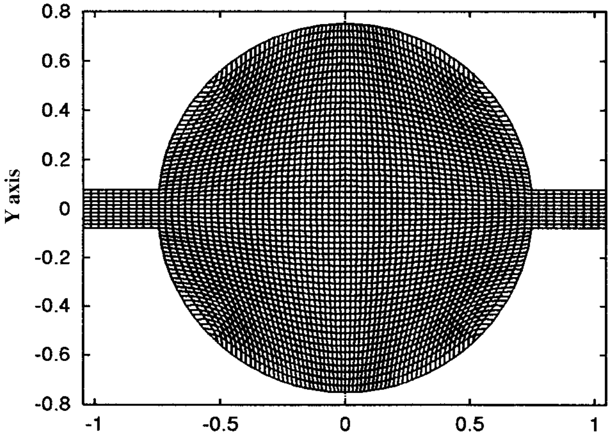

Figure 5. Finer mesh 61 × 61.

The maximum relative errors after 200 tidal cycles are presented in Table I. This test shows the accuracy and convergence of the solution, even after a long-time simulation. Finally, the CPU used for this simulation is only, 89 min for $\Delta t = 200$ s, 44 min for $\Delta\mathrm{t} = 400$ s and 22 min for $\Delta\mathrm{t} = 800$ s, on a SUN SPARC20.

5.2. *Jet-forced flow in a circular reservoir*

Next, a problem of the steady jet-forced flow in a flat-bed circular reservoir at low Reynolds number is studied. The reservoir has a radius of $R = 0.75$ m, the inlet and outlet channels both diametrically opposed of 0.157 m wide and 0.3 m long. The water depth is uniform, $h = 0.1$ m.

The Reynolds number is defined depending on the average velocity $U_I = 0.1$ m s^{-1} on the channel width b, and on the eddy viscosity A_H in the inlet. A parabolic profile of velocity is imposed here, while the elevation is null in the outlet. On the walls, no-slip boundary conditions are imposed.

Two different meshes are used: (a) 31 × 31, and a finer one (b) 61 × 61 (Figure 5). The Reynolds number is $Re = 10$ (the diffusion is $A_H = 0.00078$). The time steps used are respectively, 0.01 s and 0.02 s for the coarse and the fine mesh. The steady state was reached after $t = 80$ s.

The results of the simulations are compared with the Borthwick and Karr's numerical solution [23]. The same order of accuracy was obtained as in [23]. There is also two counter-rotating eddies on both sides of the through-flow jet in Figure 7(a)–(c). On the vorticity contours, a strong gradient occurs around the jet. It is attenuated near the walls. Large loops are generated around the inlet corners, while small loops appear around the outlet corners. Again, these characteristics are as the results of Borthwick and Karr [23] and Dennis [24].

The center of the recirculations at stagnation regions, are situated on the medium plane. The axial velocity on this plane is used to compare the present results and Borthwick and Karr's (Figure 6(a)). There is full agreement with [23] as regards the fine mesh and the same order of accuracy for the coarse mesh.

Nevertheless, Figure 7(d) and (e) show important spurious oscillations in the elevation contours.

5.3. Comments

The results obtained from the above different benchmarks prove the efficiency and the accuracy of the proposed technique for simulating coastal flows in complex geometies. Relative errors smaller than 3% in water elevation and 7% in velocity were obtained. Nevertheless, some spurious oscillations appeared in the elevation contour in Figure 7(d) and (e). If in the NS solution, these oscillations affect the pressure field only, in the SWE one, it must be remarked that they not only appear in the elevation contours, but sometime in the velocity field (see [25]). These oscillations are more significant in steady problems, such as the jet-forced flow (Figure 7), or in weakly unsteady problems [21]. Indeed, in a strongly unsteady case, such as a polar basin (Figure 3) when tidal forcing functions are imposed, these perturbations can be invisible. Nevertheless, in certain conditions, such as strong depth variations [17], these perturbations appear again [33]. In Figure 6(b), it can be remarked that the oscillation repeats over every $2\Delta x$. That represents two solutions: odd and even. As mentioned above in Section 1, this phenomenon is produced by using Chorin's projection method, in which a straightforward discretization of the continuity equation by a non-staggered mesh, causes a water elevation field decoupling. In addition, experience shows that this pollution diminishes when a finer mesh is used (Figure 6(b) and (c)). Thus, it seems that this pollution has a numerical origin. Hence, in the next section, its origin related to the algorithm will be found.

6. TREATMENT OF NUMERICAL POLLUTION

6.1. Discrete origin of the spurious oscillations

Two continue functions, ϕ and $\vec{F}$ are introduced. ϕ_h and $\vec{F}_h$ are their values at the mesh nodes, and ϕ_{hf} and $\vec{F}_{hf}$ are their values at the cell-faces. In this context, the following notations are introduced. $\vec{\nabla}_h \phi$ is the discrete form of the ϕ gradient at the mesh nodes ($\vec{\nabla}_h \phi_h|_{\mathrm{P}} = ((\phi_{\mathrm{E}} - \phi_{\mathrm{W}})/2\Delta x, (\phi_{\mathrm{N}} - \phi_{\mathrm{S}})/2\Delta y)$ in a Cartesian grid). $\vec{\nabla}_{hf} \phi_h$ is the discrete form of the ϕ gradient at the cell-faces ($\vec{\nabla}_{hf} \phi_h|_{\mathrm{e}} = ((\phi_{\mathrm{E}} - \phi_{\mathrm{P}})/\Delta x, (\phi_{\mathrm{ne}} - \phi_{\mathrm{se}})/\Delta y)$ in a Cartesian grid). $\vec{\nabla}_h \cdot \vec{F}$ is the discrete form of the $\vec{F}$ divergence at the node. It is directly linked to the neighboring cell-face values $\vec{F}_{hf}$, so note $\vec{\nabla}_h \cdot \vec{F} = \vec{\nabla}_h \cdot \vec{F}_{hf}$ ($\vec{\nabla}_h \cdot \vec{F}_{hf} = (F_{1\mathrm{e}} - F_{1w})/\Delta x + (F_{2\mathrm{n}} - F_{2\mathrm{s}})/\Delta y$ in a Cartesian grid). $A\vec{F}_h$ is the discrete form of the advection–diffusion operator ($DIV(\vec{U} \otimes \vec{F} - A_H \vec{\nabla} \vec{F})$). M is a geometrical interpolation operator that links the cell-face values with the nodal values ($\vec{F}_{hf}|_{\mathrm{e}} = M\vec{F}_h = (\vec{F}_{\mathrm{E}} + \vec{F}_{\mathrm{P}})/2$ in a Cartesian grid).

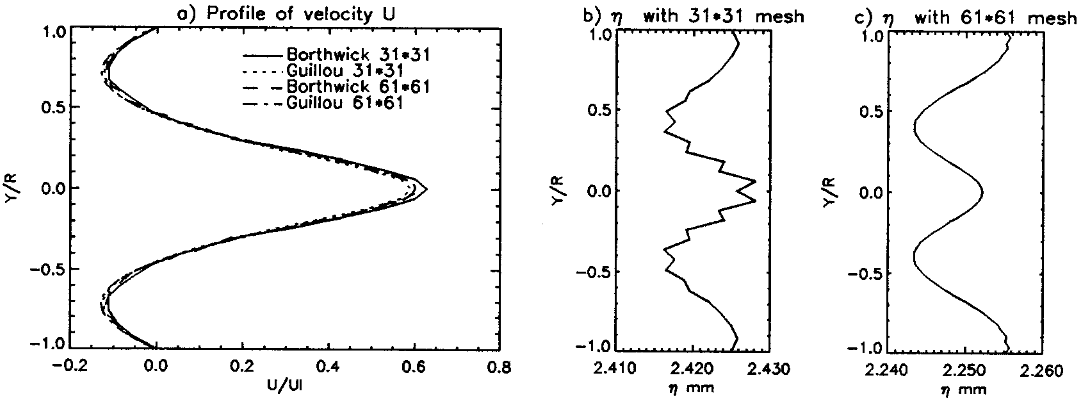

Figure 6. Velocity profile U and elevation profile on the medium plane.

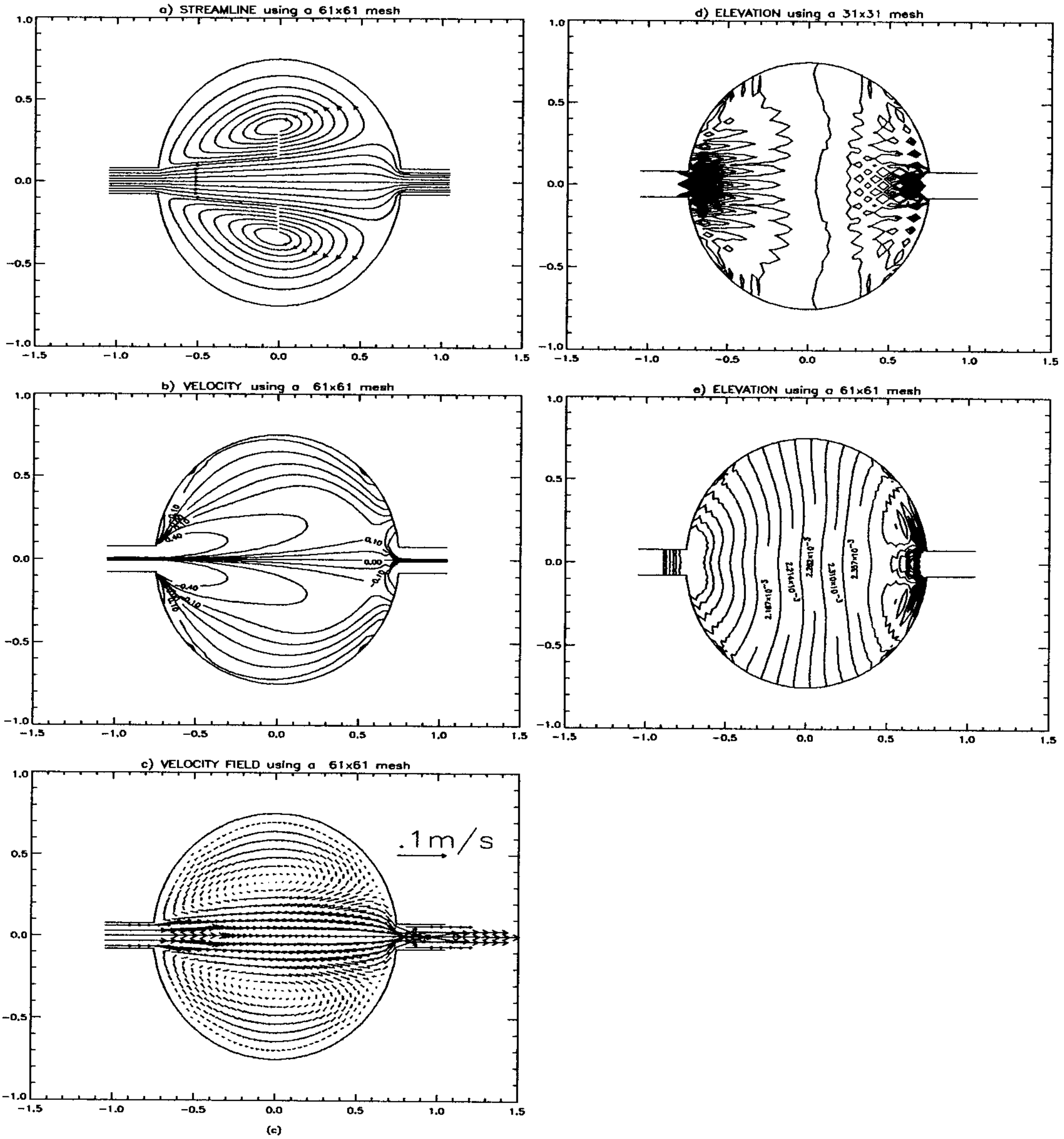

Figure 7. Prediction at $Re_I = 10$, with mesh 61 × 61 (a), (b), (c), (e) and mesh 31 × 31 (d).

In the classical Chorin's projection technique for the resolution of the Navier–Stokes equations, a specific operator $L_h(P)$ is built to calculate the pressure field P_h. This pressure operator is a combination of discrete divergence and gradient operators, such as $L_h(P) = \vec{\nabla}_h \cdot \vec{\nabla}_{hf} P_h$. In a staggered grid, this yields $L_h(P) = (P_\mathrm{E} - 2P_\mathrm{P} + P_\mathrm{W})/\Delta x^2 + (P_\mathrm{N} - 2P_\mathrm{P} + P_\mathrm{S})/\Delta y^2$ [26]. As a consequence, only one grid point system, in which the nodal values are linked with immediate neighboring ones, exists for the pressure field (see Figure 8(b)). Peyret and Taylor [26] also showed that in a non-staggered grid, a geometrical interpolation M operator must be introduced, and the pressure operator becomes, $L_h P = \vec{\nabla}_h \cdot M \vec{\nabla}_h P_h$. In a Cartesian grid, $L_h(P) = (P_\mathrm{EE} - 2P_\mathrm{P} + P_\mathrm{WW})/4\Delta x^2 + (P_\mathrm{NN} - 2P_\mathrm{P} + P_\mathrm{SS})/4\Delta y^2$. Thus, two distinct grid point systems and two distinct pressure solutions exist (see Figure 8(a)). One is linked to the odd points and the other is linked to the even points. The result solution oscillates between these two solutions; this is why these perturbations are named *odd–even oscillations*.

In order to overcome this phenomenon, a transformation of the pressure operation is necessary. Some methods exist: Dvinsky and Dukowicz [27] replaced the $\vec{\nabla}_h \cdot M\vec{\nabla}_{hf}$ operator in the pressure equation by the $\vec{\nabla}_h \cdot \vec{\nabla}_{hf}$ operator.

In the SIMPLE algorithm coupled with a non-staggered grid technique, the pressure operator, which allows one to calculate the difference between the pressure P and the intermediate pressure P^*, has the form $L_h(P) = \vec{\nabla}_h \cdot \alpha\vec{\nabla}_{hf}(P - P^*)$ (α is a scalar value depending on the method in which the velocity is calculated). Nevertheless, as mentioned by Rhie and Chow [5], the spurious oscillations still appear. They also showed that their origin stems from the implicit presence of $\vec{\nabla}_h \cdot M\vec{\nabla}_{hf}P^*$ in the discrete form of the right-hand-side of the pressure equation.

In order to find the origin of perturbations in the present scheme, the problem will first be simplified. Consider the case where the depth is constant and the friction effects are neglected. The algorithm is semi-implicit ($\theta_{\mathrm{P}} = 1$ and $\theta_{\mathrm{D}} = 0$). In this case and with the above cited notations, Equations (7)–(9) will be written as:

$$\vec{\tilde{Q}}_h^{k+1} = \vec{Q}_h^k + \Delta t A \vec{Q}_h^k, \tag{20}$$

$$\left(\frac{1}{\Delta t^2} - gH\vec{\nabla}_h \cdot \vec{\nabla}_{hf}\right)\eta^{k+1} = \frac{1}{\Delta t^2}\eta^k - \frac{1}{\Delta t}\vec{\nabla}_h \cdot \vec{\tilde{Q}}_{hf}^{k+1}, \tag{21}$$

$$\vec{Q}_h^{k+1} = \vec{\tilde{Q}}_h^{k+1} - gH\Delta t\vec{\nabla}_h\eta^{k+1}. \tag{22}$$

In this algorithm, as proposed by Dvinsky and Dukowicz [27], the operator $\vec{\nabla}_h \cdot M\vec{\nabla}_{hf}$, which is responsible of the oscillations, does not appear explicitly. So it will be found on the right-hand-side of Equation (21). Since $\vec{\tilde{Q}}_{hf}^{k+1} = M\vec{\tilde{Q}}_h^{k+1}$, and by Equations (20)–(22), Equation (21) becomes:

$$\left(\frac{1}{\Delta t^2} - gH\vec{\nabla}_h \cdot \vec{\nabla}_{hf}\right)\eta_h^{k+1} = \frac{1}{\Delta t^2}\eta_h^k + gH\vec{\nabla}_h \cdot M\vec{\nabla}_h\eta_h^k - \frac{1}{\Delta t}\vec{\nabla}_h \cdot M\vec{\tilde{Q}}_h^k - \vec{\nabla}_h \cdot MA\vec{Q}_h^k. \tag{23}$$

On the right-hand-side of Equation (23). the discrete operator $\vec{\nabla}_h \cdot M\vec{\nabla}_h$ appears. As mentioned above, it is responsible for the checkerboard. In addition, the magnitude order of this term is the same as that of $\vec{\nabla}_h \cdot \vec{\nabla}_{hf}$ on the left-hand-side. This can explain the fact that in an unsteady problem where the inertial terms are dominating, the numerical pollution probably disappears. Moreover, note that contrary to the NS solution, the velocity can be

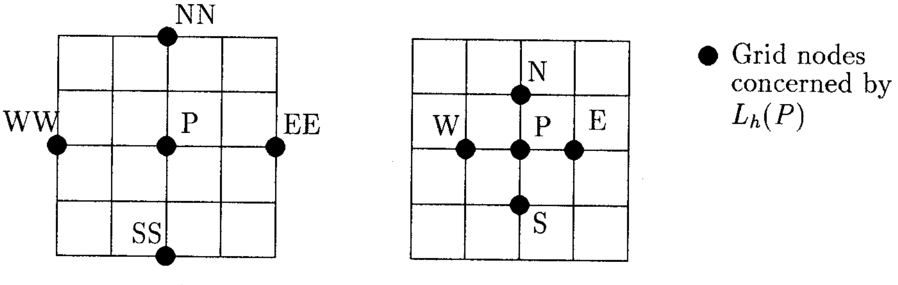

a) $L_h(P) = \vec{\nabla}_h \cdot M\vec{\nabla}_h P_h$ b) $L_h(P) = \vec{\nabla}_h \cdot \vec{\nabla}_{hf} P_h$

Figure 8. Networks of pressure operator.

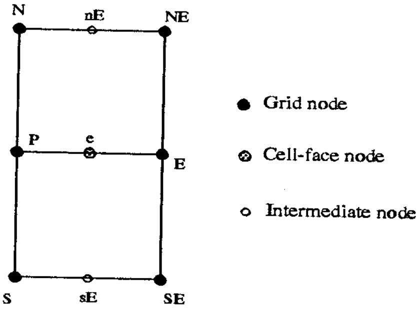

Figure 9. Intermediate control volume at the east face.

numerically polluted. This is due to the fact that in the elevation gradient term, $gH\vec{\nabla}\eta$ is non-linear, with the presence of the water depth, H.

In order to eliminate the *odd–even oscillations*, it appears necessary to replace the operator $\vec{\nabla}_h \cdot M\vec{\nabla}_h$ on the right-hand-side of the Equation (23) by $\vec{\nabla}_h \cdot \vec{\nabla}_{hf}$. To achieve this, the discharge values at the cell-faces will be interpolated using the momentum equation as an interpolating operator. This approach is akin to Deng *et al.* [10], with a difference that they used a CPI scheme (Consistent Physical Interpolation) in the SIMPLE algorithm to solve the NSE, while this paper proposes a new technique to solve the SWE by a splitting method combined with a CPI scheme.

6.2. Anti-pollution algorithm

As in Deng *et al.* [10], the advective form of the momentum equations is used to calculate the cell face velocity $\vec{u}$. Note that $\vec{\tilde{u}}^{k+1}$ is the intermediate and $\vec{u}^{k+1}$ is the final cell-face velocities at time step $(k+1)\Delta t$. The equations for the two supplementary steps are:

$$\frac{\vec{\tilde{u}}^{k+1} - \vec{u}^{k}}{\Delta t} + C^{j} \cdot \frac{\partial \vec{u}}{\partial \xi^{j}} - D_{jl} \frac{\partial^2 \vec{u}}{\partial \xi^{j}\, \partial \xi^{l}} = 0, \tag{24}$$

$$\frac{K_4 \vec{u}^{k+1} - K_5 \vec{\tilde{u}}^{k+1}}{\Delta t} + g\vec{\nabla}\eta = 0, \tag{25}$$

where $C^{j} = (1/J)\vec{b}^{j} \cdot \vec{u}^{k} - (1/J)\vec{b}^{l} \cdot (\partial/\partial\xi_{l})(1/J)\vec{b}^{j}$ and $D_{jl} = A_H(1/J^2)\vec{b}^{j} \cdot \vec{b}^{l}$.

These equations that will be integrated on the intermediate control volume $\mathscr{V}_{p1}$, linking the cell-face velocities to the nodal discharges and elevations (Figure 9).

Indeed, in Figure 9, the integration of Equation (24) over the control volume links $\vec{\tilde{u}}_{\mathrm{e}}^{k+1}$ to $\vec{u}_{\mathrm{e}}^{k}$ and $\vec{\tilde{Q}}_{M}^{k+1}$ ($M = P$, E, S, SE, N, NE), while the integration of Equation (25) links $\vec{u}_{\mathrm{e}}^{k+1}$ to $\vec{\tilde{u}}_{\mathrm{e}}^{k+1}$ and η_{M}^{k+1}, η_{M}^{k} ($M = P$, E, S, SE, N, NE). A hybrid scheme was employed on each curvilinear direction to handle the advection–diflfusion terms (see [21] for more details). The new algorithm is written as follows:

- Calculating discharge $\vec{\tilde{Q}}^{k+1}$ at the nodes by (7).
- Calculating velocity $\vec{\tilde{u}}^{k+1}$ at the faces by (24).
- Calculating elevation η^{k+1} at the nodes by (8) with $H\vec{\tilde{u}}^{k+1}$ in place of $\vec{\tilde{Q}}^{k+1}$.
- Calculating discharge $\vec{Q}^{k+1}$ at the nodes by (9).
- Calculating velocity $\vec{u}^{k+1}$ at the faces by (25).

Since Equations (24) and (25) have been added to the algorithm, the use of a geometrical interpolation to obtain the cell-face discharge $\vec{\tilde{Q}}_{hf}^{k+1}$ is not necessary. When using these supplementary steps, and the notation of Section 6.1, Equation (23) becomes:

$$\left(\frac{1}{\Delta t^2} - gH\vec{\nabla}_h\cdot\vec{\nabla}_{hf}\right)\eta_h^{k+1} = \frac{1}{\Delta t^2}\eta_h^k + gH\vec{\nabla}_h\cdot\vec{\nabla}_{hf}\eta_h^k - \frac{1}{\Delta t}\vec{\nabla}_h\cdot\vec{Q}_{hf}^k - \vec{\nabla}_h\cdot A\vec{Q}_h^k. \tag{26}$$

Clearly, the unexpected operator $\vec{\nabla}_h\cdot M\vec{\nabla}_h$ on the right-hand-side of (23) had been replaced by $\vec{\nabla}_h\cdot\vec{\nabla}_{hf}$ in (26). The numerical origin of the pollution has been shown and a method proposed to avoid it. Hence, it is yet to be shown that the numerical solution is free from oscillation.

6.3. Checking of the new algorithm

The new algorithm was applied to calculate the free-surface flow in the circular reservoir as presented in Section 5.3. Figure 10 presents the computed water level contour map. Clearly, the spurious oscillations have completely disappeared.

A steady laminar and incompressible flow across a staggered tube bank, which was first proposed by Wakisaka *et al.* [28], is also used to validate the method. This is in fact a bi-dimensional Navier–Stokes benchmark in which there does not exist a free water surface as in shallow water problems. However, we can remark that a bi-dimensional shallow water problem will have the same behavior as a bi-dimensional Navier–Stokes one if the non-slip conditions should be imposed on the water surface (no-wind) and on the bottom (no-bed friction).

The transverse and longitudinal distances between two tubes are 15.9 and 25 mm, while the tube diameter is 12.7 mm. The water depth is 20 mm. The flow is at the Reynolds number $Re = 140$, which is calculated on the tube diameter and the mean velocity in the medium gap.

Figure 11(a) shows the 71 × 30 calculating grid for a symmetrical pair of the staggered tube bank. As in the NS benchmark [28], a parabolic velocity profile is imposed in the inlet, while pressure (a surface elevation) is fixed in the outlet. No-slip boundary conditions are fixed on the water surface, on the bottom, and on the tube walls. Figure 11(c) and (d) present the surface elevation map and the streamlines obtained from the model. It can be seen that the elevation is free from oscillations. In Figure 11(b), the profiles of the computed streamwise velocity components (continuous lines) are compared with the experimental data [29] (discrete points). Obviously, the computed values of the current velocity are in agreement with the experimental ones.

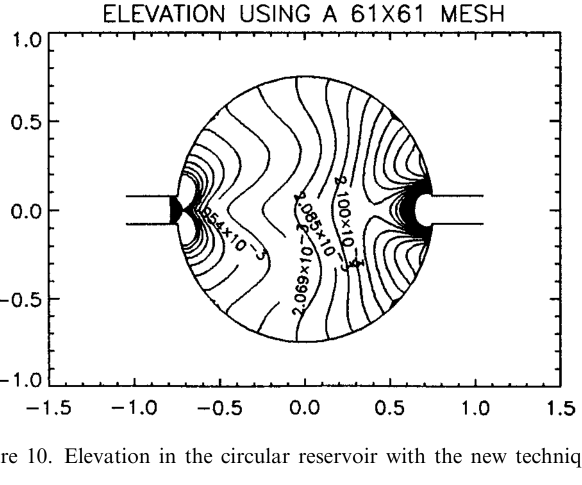

Figure 10. Elevation in the circular reservoir with the new technique.

a) 71*30 mesh

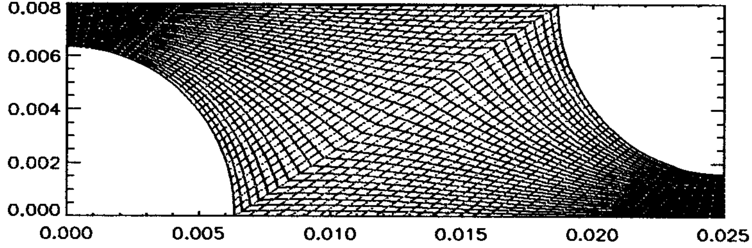

b) Profile of streamwise velocity component

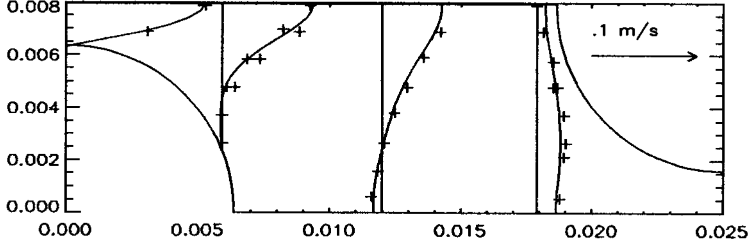

c) Surface elevation

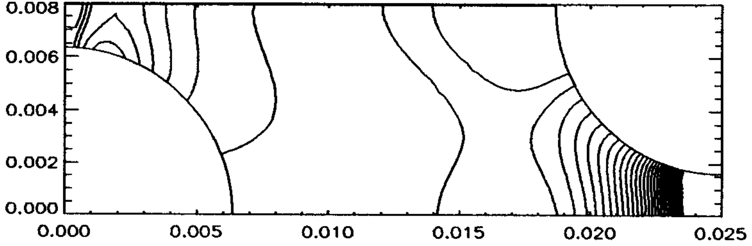

d) Calculated streamlines

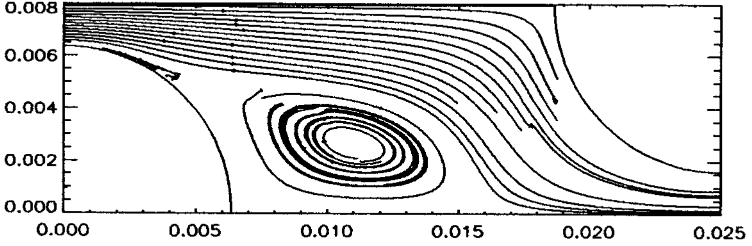

Figure 11. Profiles of streamwise velocity component (computed: continued line, experimental: symbols), free surface elevation and calculated stramline at $Re = 140$.

Evidently, the preceding benchmarks approve the proposed model in a quantitative way. In the next section, a more complex benchmark is presented to test the model capacity. That is the flow passed over two circular piers in a channel. This benchmark was first proposed by Galland *et al.* [15].

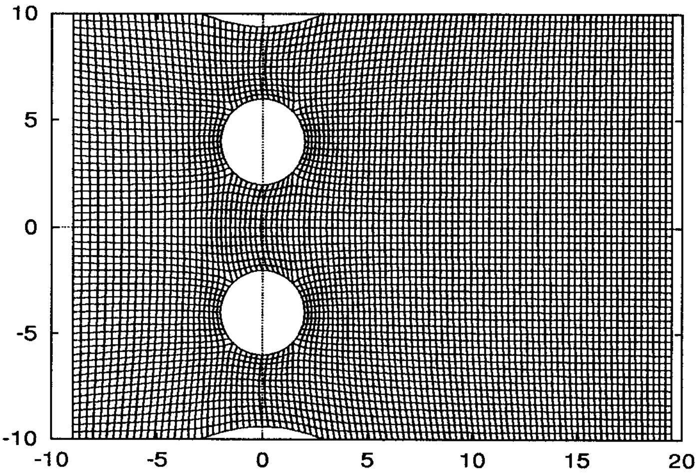

Figure 12. 100 × 61 mesh in the physical plane.

6.4. Flow passed over two circular piers

The flow passing along two 2 m diameter circular piers in a 30 m long and 20 m wide channel will be studied. The piers are axisymetrically situated 4 m away from the channel axis (Figure 12). The water depth is uniform $h = 4$ m. A discharge, $Q = 61$ m^3 s^{-1}, uniformly distributed over the whole section, is imposed at the inlet. There, the water elevation will be specified by the radiation constraint (see Arnold [30]). At the outlet, the zero water level is fixed, while the discharge will be calculated by a radiation condition. Finally, a no-slip boundary condition is prescribed at the lateral walls. In this simulation, the constant diffusivity is $A_H = 0.001$ m^2 s^{-1}, Darcy's parameter is $C_f = 7.725 \times 10^{-3}$, the weight coefficients are $\theta_P = \theta_D = 0.5$. This benchmark was proposed by Galland *et al.* [15].

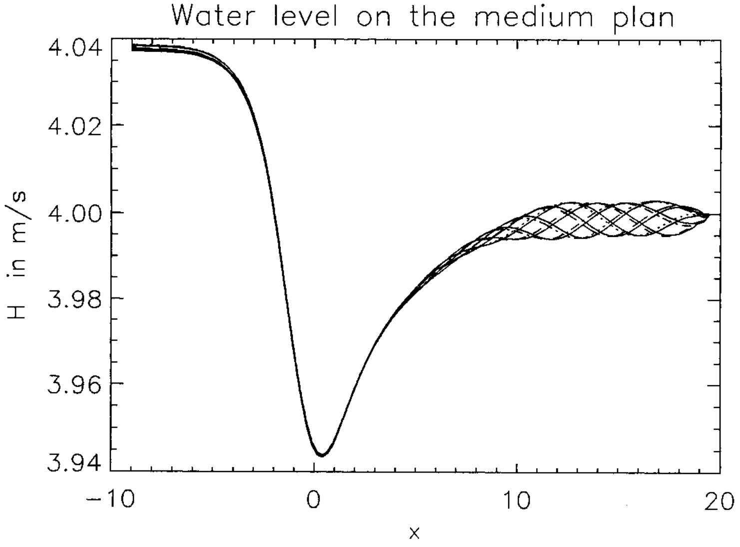

Figure 13. Elevation on the river axis for $t = 720 + (18, 22, 24, 24, 26, 28, 30, 32, 34)$ s.

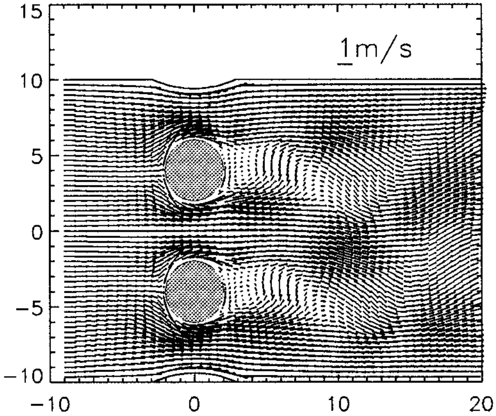

a) Velocity at t=720s

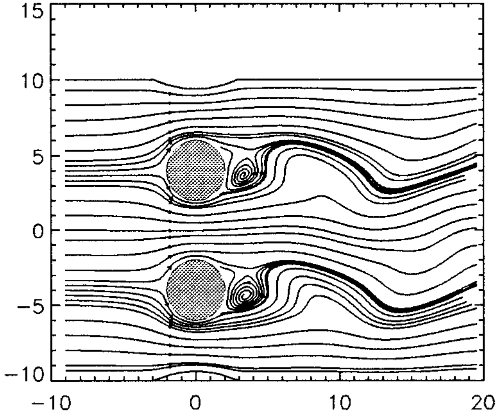

b) Streamline at t=720s

Figure 14. Flows in a river with piers: velocity and streamline at $A_H = 0.001$ m^2 s^{-1}.

A uniform flow is chosen as the initial condition. Initially, a time step of 0.2 s is used in order to reach a nearly steady flow upstream of the piers. Next, the simulation will run using a time step of 0.1 s to obtain the more accurate results.

Figure 14 presents the velocity field and its streamlines calculated by the new algorithm. Clearly, the flow is quasi-stationary upstream of the piers. Downstream, Von Karman's vortices of period $T = 19.3$ s occur (Figure 13). Moreover, note that the flow pattern in Figure 14 is the same as the one obtained by Galland [15]. The water level rise at the inlet, calculated by the proposed model, was compared with the one given by Nicollet [31]. A relative error of 2% is obtained. In addition, Strouhal's number of the Karman vortex oscillation is obtained from the present results, and is $St = 0.27$.

Figure 15 presents the water elevation contour map calculated by the new algorithm. Thanks to the anti-pollution technique, the spurious oscillations appearing in Guillou *et al.* [32] and also in Galland *et al.* [15] were completely removed from the elevation field.

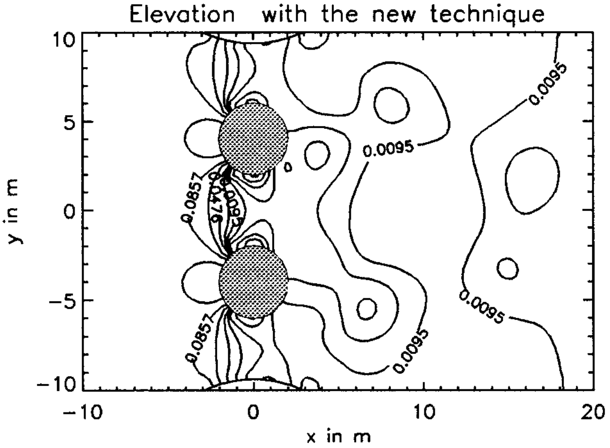

Figure 15. Elevation in a river with piers.

7. CONCLUSION

In recent years, there has been several research papers that discuss and handle the checkerboard using a non-staggered grid technique, but they are only used to solve the Navier–Stokes equations. This paper is the first that discusses the checkerboard occurring in coastal and estuarine modeling and has found the checkerboard. The *Inf–sup* condition (Brezzi and Fortin [16], Guermond [7,8]) has not been fully discussed as it falls outside the scope of the paper. However, Guillou [21] has mathematically shown that if the *Inf–sup* condition is necessary to insure the unicity of the Navier–Stokes solution and to avoid the checkerboard, this condition is not required to guarantee the existence of the shallow water solution. In this context, the spurious oscillations will still be produced in the elevation field and even in the velocity. In order to avoid them, a new algorithm is proposed in the present paper. An approach similar to CPI [10] is also introduced in the algorithm to calculate shallow water flows by a fractional step method (see Nguyen and Ouashine [18]). The numerical results computed by the present algorithm for the benchmarks in Sections 5.3 and 6.3 showed no spurious oscillation in elevation and velocity fields. The efficiency of the present algorithm is proven.

REFERENCES

1. K.C. Karki and S.V. Patankar, *AIAA J.*, **27**, 1167 (1989).
2. K.D. Nguyen, J.M. Legouez, H.Viviand and M. Cazalens, 'Simulation of reactive flow in complex geometries', *2nd Int. Conf. on Industrial and Applied Mathematics*, 1991.
3. S.V. Patankar, *Numerical Heat Transfer and Fluid Flow*, Hemisphere Publishing, New York, 1980.
4. Y. Zang, R.L. Street and J.R. Koseff, 'A composite-multigrid method for solving unsteady incompressible Navier–Stokes equations in complex geometries', *7th Int. Conf. on Numerical Methods in Laminar and Turbulent Flows*, Stanford, CA, 1991, p. 1485.
5. C.M. Rhie and W.L. Chow, 'Numerical study of the turbulent flow passed an airfoil with trailing edge separation', *AIAA J.*, **21**, 1525–1532 (1983).
6. A.J. Chorin, 'Numerical solution of the Navier–Stokes equations', *Math. Comput.*, **22**, 745–762 (1968).
7. J.L. Guermond, 'Approximation des équations de Navier–Stokes instationnaires par des méthodes de projection', *Notes et Documents LIMSI*, **30**, 1993.
8. J.L. Guermond, 'Approximation inconditionnellement stable par elements finis et méthode de projection pour les équations de Navier–Stokes instationnaires', *Notes et Documents LIMSI*, **6**, 1995.
9. Y. Zang, R.L. Street and J.R. Koseff, 'A non-staggered grid, fractional step method for time-dependent incompressible Navier–Stokes equations in curvilinear co-ordinates', *J. Comput. Phys.*, **114**, 18–33 (1994).

10. G.B. Deng, J. Piquet, P. Queutey and M. Visonneau, 'Incompressible flow calculations with a consistent physical interpolation finite volume approach', *Comput. Fluids*, **23**, 1029–1047 (1994).
11. J.P. Benque, J.A. Cunge, J. Feuillet *et al.*, 'New method for tidal current computation', *J. Waterway, Port, Coastal, Ocean Div. ASCE*, **108**, 396–417 (1982).
12. A.F. Blumberg and L.H. Kantha, 'Open boundary condition for circulation models', *J. Hydraul. Eng. ASCE*, **111**, 237–255 (1985).
13. R.A. Falconer, 'Numerical modeling of tidal circulations in harbours', *J. Waterway, Port, Coastal Ocean Div.*, **106**, 31–48 (1980).
14. P. Nielsen and O. Skovgaard, 'The effect of using non-orthogonal boundary-fitted grids for solving the shallow water equations', *Int. J. Numer. Methods Fluids*, **11**, 177–188 (1990).
15. J.C. Galland, N. Goutal and J.M Hervouet, 'Telemac: A new numerical model for solving shallow water equations', *Adv. Water Resources*, **14**, 138–148 (1991).
16. F. Brezzi and M. Fortin, *Mixed and Hybrid Finite Element Methods*, Springer, New York, 1991.
17. J.M. Hervouet, J.M. Jamin and E. Barros, 'Refined flow modelling in coastal areas', in C.A. Brebbia (ed.), *Computer Modelling of Seas and Coastal Regions II, COASTAL95*, Computational Mechanics Publications, Southampton, UK, 1995, pp. 3–10.
18. K.D. Nguyen and A. Ouashine, 'A 2D numerical study on the general circulation in the straits of Dover', *J. Waterway, Port, Coastal, Ocean Eng.*, **123**, 8–15 (1997).
19. R.M. Beam and R.F. Warming, 'Alternating direction implicit methods for parabolic equations with a mixed derivative', *SIAM. J. Sci. Statist. Comput.*, **1**, 131–159 (1980).
20. R. Temam, *Navier–Stokes Equations*, North-Holland, Amsterdam, 1977.
21. S. Guillou, 'Modélisation des ecoulements côtiers et estuariens. Etude mathématique et applications en co-ordonnées généralisées', *Doctoral Thesis*, Université Pierre et Marie Curie, Paris, 1996.
22. C.L. Chen, 'Analytic solutions for tidal model testing', *J. Hydraul. Eng. ASCE.*, **115**, 1707–1713 (1989).
23. A.G.L Borthwick and E.T. Karr, 'Shallow flow modelling using curvilinear depth-averaged streamfunction and vorticity transport equations', *Int. J. Numer. Methods Fluids*, **17**, 417–445 (1993).
24. S.C.R. Dennis, 'Application of the series truncation method to two-dimensional internal flows', in *Proc. 4th Int. Conf. on Numerical Methods in Fluid Dynamics*, University of Colorado, CO, Springer, New York, 1974, pp. 146–151.
25. S. Guillou and K.D. Nguyen, 'Modélisation numérique des écoulements côtiers par une technique de volumes finis en co-ordonnes généralisées', *Actes du 12e Congrés Français de mécanique*, Strasbourg, France, 1995, pp. 285–288.
26. R. Peyret and T.D. Taylor, *Computational Methods for Fluid Flow*, Springer, New York, 1983.
27. A.S. Dvinsky and J.K. Dukowicz, 'Null-space free methods for the incompressible Navier–Stokes equations on non-staggered curvilinear grids', *Comput. Fluids*, **22**, 685–696 (1993).
28. T. Wakisaka, T. Yaso and Y. Shimamoto, 'A finite volume method for predicting fluid flows through passages with obstacles and moving boundaries', *5th Int. Symp. on Computational Fluid Dynamics*, vol. III, Sendai, 1993, pp. 285–290.
29. S. Nowshirawa *et al.*, *Aerospace Eng. Dept. Rep.*, Case Institute of Technology, Case Western Reserve University, 1983.
30. R.J. Arnold, 'An improved open boundary condition for a tidal model of bass strait', in J. Noye (ed.), *Numerical Modelling: Applications to Marine Systems*, Elsevier Science, Amsterdam, 1987, pp. 145–158.
31. G. Nicollet, 'Hydraulique des ouvrages de franchissement des vallées fluviales', *La Houille Blanche*, **4**, 289–308 (1982).
32. S. Guillou, J. Sanchez-Hubert and K.D. Nguyen, 'Oscillations parasites dans la résolution des equations des eaux peu profondes', *Worshop: Modélisation en Dynamique des fluides géophysiques*, Lille, France, 1996.
33. S. Guillou and K.D. Nguyen, 'A collocated finite volume technique for 2D coastal flow in arbitrary geometry', in C.A. Brebbia (ed.) *Computer Modelling of Seas and Coastal Regions II, COASTAL95*, Computational Mechanics Publications, Southampton, UK, 1995, pp. 39–47.
34. F.H. Harlow and J.E. Welch, *Phys. Fluids*, **8**, 2182 (1965).